ADVANCED ENERGY MATERIALS
www.advenergymat.de

Combined In Situ X-Ray Spectroscopic and Theoretical Study on Trimetal Synergistic Enhancement of Water Oxidation

Yalei Fan, Xubin Ye, Jing Zhou, Dabiao Lu, Chang-Yang Kuo, Yu-Cheng Huang, Ting-Shan Chan, Chien-Te Chen, Youwen Long, Jian-Qiang Wang,* Zhiwei Hu,* and Linjuan Zhang**

Electrochemical water-splitting is vital in energy storage and conversion applications. However, the sluggish kinetics of the oxygen evolution reaction (OER) hinders the electrochemical water-splitting. Therefore, developing efficient catalysts and understanding the OER mechanism are highly desirable. This study successfully synthesized a new quadruple perovskite oxide $CaCu_3Co_2Ru_2O_{12}$ (CCCRO) catalyst exhibiting high OER activity with overpotential 198 mV at 10 mA cm^{-2}, a Tafel slope of 37 mV dec^{-1}, and long-term operational stability with a current density of 500 mA cm^{-2} for >500 h. The in situ X-ray absorption near-edge structure (XANES) indicated that a part of high-spin (HS) Co^{3+} ions and low-spin (LS) Ru^{5+} ions transitioned to the tetravalent Co (IV) and hexavalent Ru (VI) valence states under OER. However, the Cu^{2+} valence state remained unchanged. Furthermore, the density functional theory (DFT) calculations reveal that the lattice-oxygen oxidation mechanism (LOM) rather than conventional adsorbate evolution mechanism (AEM) is responsible for high OER activity in Ru (VI)-O-Co (IV) network, and that the Cu(A')/Co(B)/Ru(B') three sites synergistically facilitate the OER activity for CCCRO.

1. Introduction

The increased carbon dioxide emissions due to the rapidly growing energy demand have led to environmental pollution and global warming, making the pursuit of renewable and clean energy sources imperative.[1–4] Electrochemical water-splitting, powered by renewable electricity derived from wind and solar energies, is a promising and sustainable approach for producing clean hydrogen fuel from aqueous solutions.[5–7] Additionally, electrochemical water-splitting involves two key reactions: anodic oxygen evolution reaction (OER) and cathodic hydrogen evolution reaction (HER). The OER is the bottleneck in the electrochemical water splitting due to the sluggish kinetics of the four electron-coupled proton transfer process.[8,9] Although the oxides of precious metals, like ruthenium (Ru) and iridium (Ir) are considered the most effective commercial OER electrocatalysts, their widespread practical applications are hindered due to their scarcity and exorbitant costs.[10–13] Therefore, it is highly desirable to develop efficient OER catalysts with abundant resources, low costs, high activity, and excellent stability and to understand the underlying OER mechanism. Particularly, the advancement of catalysts

Y. Fan, J.-Q. Wang, L. Zhang
Key Laboratory of Interfacial Physics and Technology, Shanghai Institute of Applied Physics
Chinese Academy of Sciences
Shanghai 201800, P. R. China
E-mail: wangjianqiang@sinap.ac.cn; zhanglinjuan@sinap.ac.cn

Y. Fan, J.-Q. Wang, L. Zhang
University of Chinese Academy of Sciences
Beijing 100049, P. R. China

X. Ye, D. Lu, Y. Long
Beijing National Laboratory for Condensed Matter Physics
Institute of Physics
Chinese Academy of Sciences
Beijing 100190, P. R. China
E-mail: ywlong@iphy.ac.cn

J. Zhou
Zhejiang Institute of Photoelectronics and Zhejiang Institute for Advanced Light Source
Zhejiang Normal University
Jinhua, Zhejiang 321004, P. R. China

C.-Y. Kuo, Y.-C. Huang, T.-S. Chan, C.-T. Chen
National Synchrotron Radiation Research Center
Hsinchu, Taiwan 300092, R. O. China

C.-Y. Kuo
Department of Electrophysics
National Yang Ming Chiao Tung University
Hsinchu, Taiwan 300025, R. O. China

Z. Hu
Max Planck Institute for Chemical Physics of Solids
01187 Dresden, Germany
E-mail: Zhiwei.Hu@cpfs.mpg.de

The ORCID identification number(s) for the author(s) of this article can be found under https://doi.org/10.1002/aenm.202404599

DOI: 10.1002/aenm.202404599

with large-scale industrial applications in alkaline solutions is indispensable for expediting full-scale hydrogen production through water electrolysis.

Perovskite-type metal oxides with the general ABO_3 formula, where A = alkaline earth or rare earth metals and B = transition metals (TMs), structural stability, and high electronic conductivity have received increasing attention in water splitting.[14–17] The multi-elements synergistic effect is a useful way to boost the OER activity. Doping nonprecious 3d TM ions in the electrocatalyst ABO_3 (B = Ru and Ir) can remarkably enhanced the OER activity and at the same time reduce the usage of Ru and Ir ions.[18–23] For example, $La_{1.5}Sr_{0.5}NiMn_{0.5}Ru_{0.5}O_6$ exhibited a 10 mA cm^{-2} current density at 1.66 V, comparable to that of RuO_2 but with significantly reduced precious metal content.[18] The synergistic effect between the Co and Ir ions in $Sr_2CoIrO_{6-\delta}$ led to a low overpotential of 210 mV at a 10 mA cm^{-2} current density, which was significantly superior to the $SrCoO_{3-\delta}$ and $SrIrO_{3-\delta}$ catalysts.[19] $CaCu_3Ir_4O_{12}$ had a mass activity reaching about 50.2 A g^{-1} at 1.50 V, about three times of IrO_2.[20] Although $CaCu_3Ir_4O_{12}$ had OER inactive-Cu^{2+} ions, the synergistic effect due to Cu^{2+} ions through orbital mixing between localized Cu 3d orbitals and much expanded Ir 5d states effectively enhanced the OER performance. Therefore, the synthesis of complex multi-metal oxides is a promising approach for the reduced usage of precious metals and enhanced OER performance.

In comparison to precious metals, Co-based electrocatalysts have a lower price. Moreover, Co ions not only possess various oxidation states such as +2, +3, and +4, but also have spin degree of freedom, namely Co^{3+} and Co^{4+} ions can have high-spin (HS), low-spin (LS) even Intermediate-spin (IS) states. Therefore, Co compounds are extensively used in electrocatalysis.[7,19,24,25] When Co is incorporated into Ru-based materials, the synergistic effects between Co and Ru can effectively improve the OER performance.[25] The $Ru/LiCoO_2$ single atom catalyst exhibited enhanced conductivity and reduced oxygen adsorption energy due to strong electron coupling between Ru and Co sites, leading to a low overpotential of 247 mV at a 10 mA cm^{-2} current density.[25]

Theoretically, the conventional adsorbate evolution mechanism (AEM) cannot overcome the limitations of the linear proportional relationship of key intermediates, like *O, *OH, and *OOH, and fails to represent the low overpotential of catalysts for TMs with a strong TM d-O 2p covalent property, such as Fe (IV), Co (IV), and Ni (IV) states.[26,27] Recent studies have unveiled the pivotal role of lattice oxygen in water oxidation processes through the formation of surface oxygen vacancies (O_V) and the repair of specific oxides and hydroxide materials, referred to as lattice-oxygen oxidation mechanism (LOM).[28,29] The LOM-based OER decoupled the proton and electron transfer, circumventing the constraints imposed by the linear proportional AEM to reduce the overpotential and energy consumption. Many high valence state oxides showed the lattice-oxygen participation of OER.[30–32] For example, the $Fe_2O_3@CeO_2$-O_V catalyst, featuring a significant presence of O_V and binding heterojunctions, effectively activated the lattice oxygen.[30] Moreover, this activation shifted the reaction pathway from AEM to LOM, impressively reducing the overpotential with only 172 mV required at 10 mA cm^{-2}. A part of Li ions was removed from the $Li_2Co_2O_4$[31] and $LiNiO_2$[32] catalysts during the OER, and high-valence Co (IV) and Ni (IV) species were produced, which activated the surface lattice oxygen and enabled the direct O—O coupling between the lattice oxygen and the *O intermediates to optimize the OER activity.

This study reported an electrocatalyst of complex perovskite oxide $CaCu_3Co_2Ru_2O_{12}$ (CCCRO), where the TM ions of Cu, Co, and Ru were expected to boost the OER performance synergistically. This electrocatalyst exhibited an excellent OER performance in alkaline solutions, with an ultralow overpotential of 198 mV for a current density of 10 mA cm^{-2}, ranking the highest performance among Co-Ru based catalysts. First, in situ X-ray absorption near-edge structure (XANES) was measured to explore the valence states of Cu, Co, and Ru as a function of the applied potential starting from $Cu^{2+}/Co^{3+}/Ru^{5+}$ determined using the ex situ $L_{2,3}$-edge soft X-ray absorption spectroscopy (sXAS) spectra. Then, in situ extended X-ray absorption fine structure (EXAFS), in situ synchrotron radiation (SR)-based X-ray diffraction (XRD), and in situ Raman spectroscopy were employed to study the possible structural modification under OER. Finally, the OER mechanism in this complicated catalyst with three TMs was expatiated using the density functional theory (DFT).

2. Results and Discussion

2.1. Crystal Structure and Morphology

The ruthenate oxide CCCRO belonged to the typical cubic A-site ordered quadruple perovskite compound $AA'_3B_4O_{12}$, with a 2 × 2 × 2 superstructure of simple cubic perovskite ABO_3. As shown in **Figure 1a**, one Ca^{2+} and three Cu^{2+} ions occupy A-sites in order, while the Co^{3+} and Ru^{5+} ions formed the corner-share $(Co/Ru)O_6$ octahedra at B-sites randomly. A solid-state reaction method was used to successfully prepare the CCCRO sample, whose structure was characterized using SR/lab-based XRD. As shown in Figure 1b, the Rietveld refinement of the lab-based XRD pattern revealed that CCCRO adopted the *Im*-3 space group. Additionally, the lattice parameter was a = 7.30121(1) Å, with no observable impurity phases (Table S1, Supporting Information). Moreover, based on the $CaCu_3Ru_4O_{12}$ reference (ICSD PDF#95715), it is observed that the peaks shift to the right at the high angular position (Figure S1, Supporting Information), indicating the lattice shrinkage, which is caused by the smaller ionic radius of Co ions and the higher oxidation state of Ru (as confirmed by XAS, shown below) when Co is partially replacing replaced Ru cations. Additionally, the crystalline phase of the prepared CCCRO was characterized using SR-based XRD. Moreover, the SR-based XRD patterns of CCCRO exhibited a strong correlation with the standard $CaCu_3Ru_4O_{12}$ spectra (ICSD PDF#95715) (Figure S2, Supporting Information). Furthermore, pure phase $CaCu_3Ru_4O_{12}$ and Sr_2CoRuO_6 samples were synthesized, and their lab-based XRD patterns and the Rietveld refinement are shown in Figures S3 and S4 (Supporting Information) as comparison catalysts for CCCRO catalyst. Transmission electron microscopy (TEM) was used to understand the morphology of the CCCRO catalyst. The morphology of the pristine CCCRO particles showed an average particle size of ≈50 nm (Figure S5, Supporting Information). As shown in the high-resolution TEM (HRTEM) image in Figure 1c, the lattice fringes of CCCRO had a plane d-spacing of 0.264 nm corresponding to its (220) planes. The perovskite

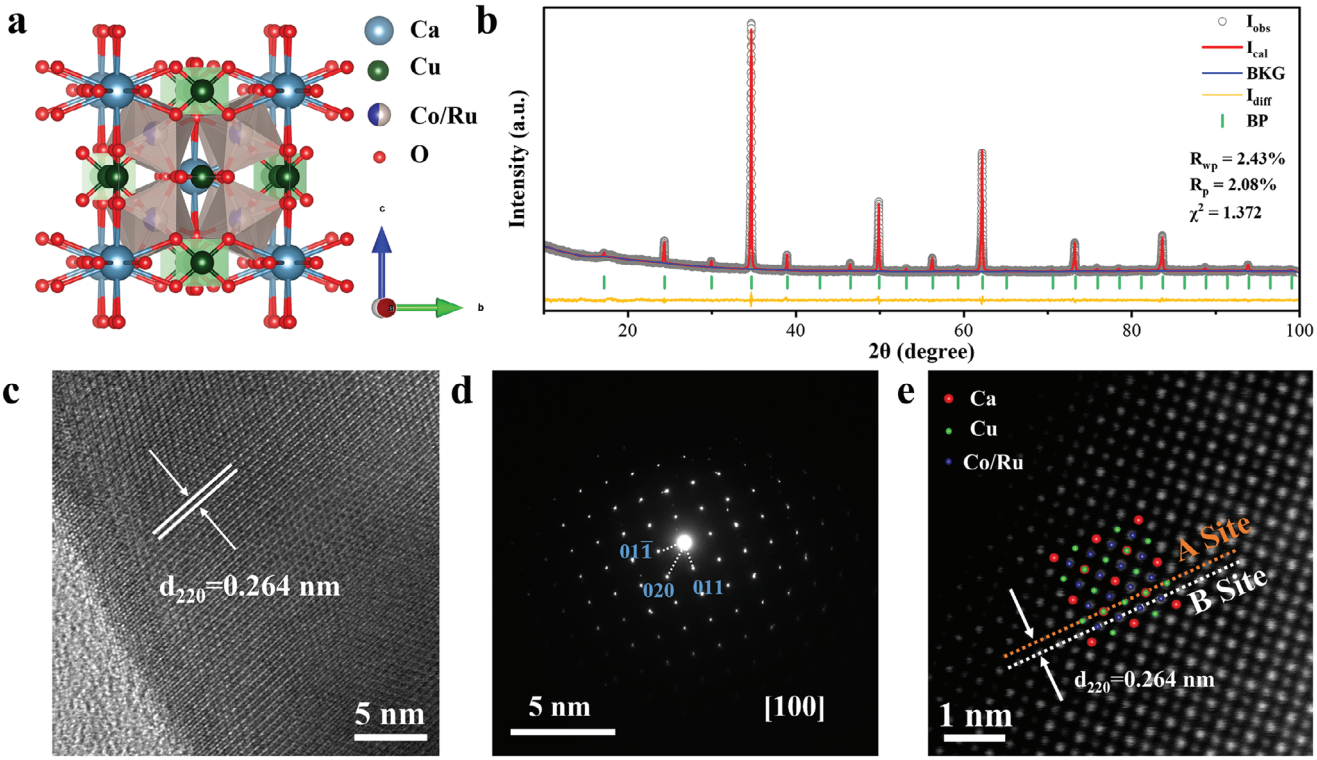

Figure 1. Structural characterization for CCCRO. a) Crystal structural model. b) Refined. XRD profile. c) HRTEM image. d) SAED pattern along the [110] direction. e) Atomic-resolution HAADF-STEM image. The red, green, and blue dots represent the Ca, Cu, and Co/Ru atoms, respectively.

crystal matrix on the surface was well-preserved with no discernible amorphous layer. As shown in the selected area electron diffraction (SAED) pattern of CCCRO recorded along the [100] zone axis in Figure 1d, CCCRO had good crystallinity. Furthermore, as shown in the high-angle annular dark-field scanning transmission electron microscopy (HAADF-STEM) images in Figure 1e, the atomic image of CCCRO was in excellent agreement with the theoretical structure. The atomic image in Figure 1e depicts the (001) planes, where atoms at A site and B site were arranged alternately. As shown in Figure S6 (Supporting Information), the elemental content of the CCCRO sample was characterized using energy-dispersive X-ray (EDX) spectroscopy. The results demonstrated that the constituent elements were uniformly distributed in CCCRO, element segregation did not occur, and the atomic ratios of Ca/Cu/Co/Ru/O adhered to the anticipated stoichiometry (Table S2, Supporting Information).

2.2. Electronic Structure

It is well known that the energy position and multiplet spectral feature of sXAS at the $L_{2,3}$-edge of 3d TMs are highly sensitive to the valence states,[33,34] spin states,[35,36] and local environment[37,38] of the 3d TM ions. The Cu $L_{2,3}$-edge spectra of CCCRO and references $Cu^{2+}O$ and $Cu^{+}{}_2O$ for comparison are shown in **Figure** 2a.[39] The white line peak for CCCRO and CuO had the same energy position, suggesting a +2 valence state for Cu in CCCRO. As depicted in Figure 2b, the energy position and shape of the Co $L_{2,3}$-edge spectra of CCCRO and Sr_2CoRuO_6 had a close resemblance, suggesting the presence of Co as a HS-Co^{3+} state in CCCRO.[40] Furthermore, ascertaining the valence state of Ru was imperative to elucidate the definitive chemical formula of CCCRO. As shown in Figure 2c, the white line peak for CCCRO and Sr_2CoRuO_6 had the same positioning in the Ru L_3-edge spectra, indicating a +5 oxidation state for Ru in CCCRO to fulfill the charge balance requirement.

Additionally, the XANES at the TM *K*-edge is sensitive to the valence state of the TM ions.[41,42] The Cu *K*-edge XANES spectra of CCCRO, CuO, Cu_2O, and the Cu foil are shown in Figure 2d. The absorption edge of CCCRO (at a normalized intensity of 0.8) was at the same position as that of CuO, providing further evidence for Cu^{2+} in CCCRO. Additionally, the *K*-edge XANES of Co and Ru are shown in Figure 2e,f. Evidently, the absorption edge of CCCRO were at the same position as those of $LaCoO_3$ and Sr_2CoRuO_6 in Co and Ru *K*-edge XANES, respectively, further confirming the $Cu^{2+}/Co^{3+}/Ru^{5+}$ valence states in CCCRO. It is well known that the EXAFS is extremely sensitive to the local environment of metal ion, including the bond length, coordination number, and degree of disorder.[19,30,43] The EXAFS analysis of CCCRO is presented in Figure S7 (Supporting Information). Based on the best fitting results of Fourier transform (FT)-EXAFS spectra, we can conclude that Cu adopted a CuO_4 coordination structure in CCCRO, while the Co and Ru ions exhibited an octahedral coordination reflecting their atomic positions (Figure 2g–i; Figures S8 and S9 and Table S3, Supporting Information). However,

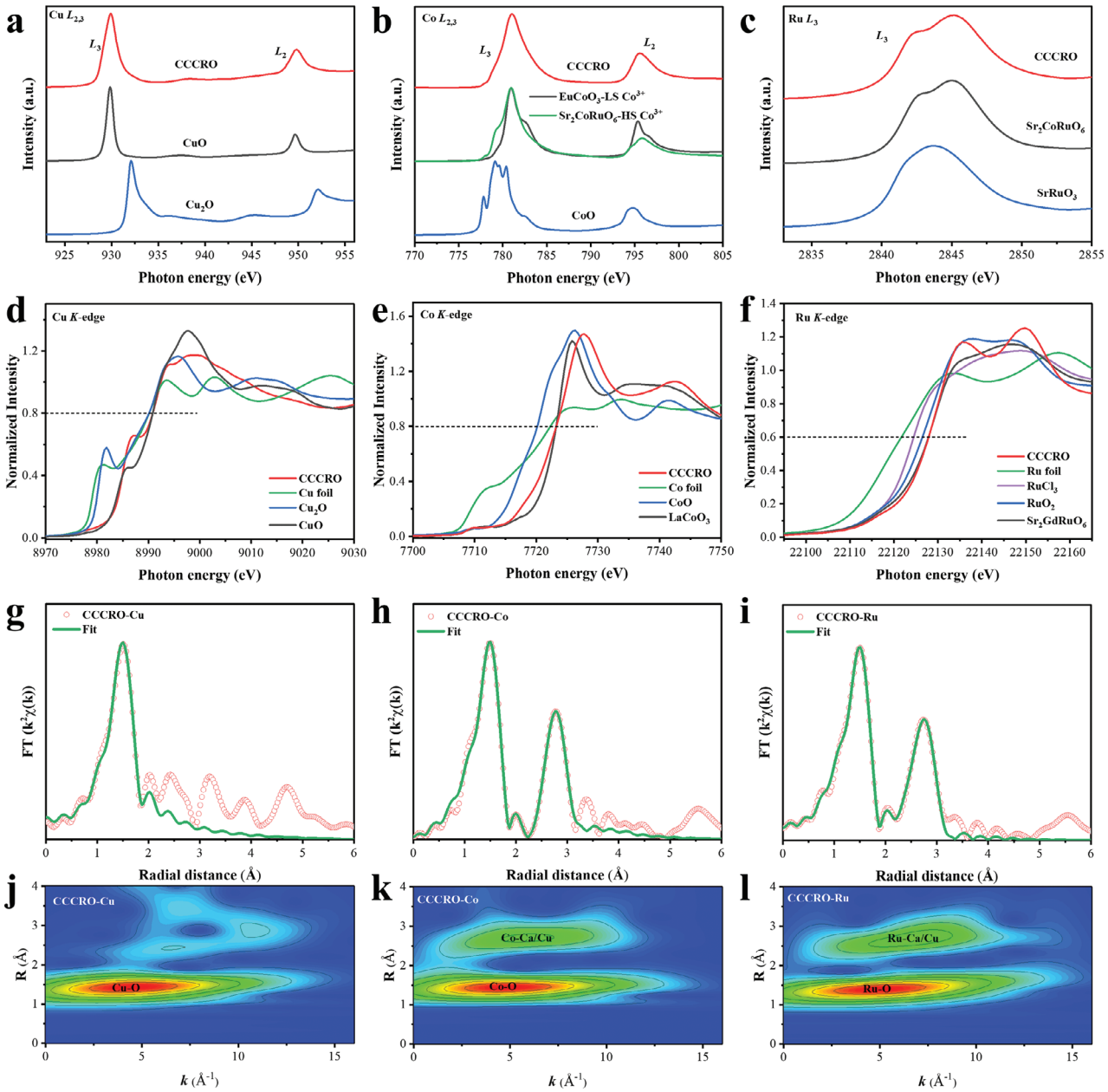

Figure 2. Characterization of valence and coordination structures. a) Cu $L_{2,3}$-edge spectra of CCCRO (red line) and references $Cu^{2+}O$ (black line) and $Cu^{+}{}_2O$ (blue line). b) Co $L_{2,3}$-edge spectra of CCCRO (red line) and references LS-Co^{3+} ($EuCo^{3+}O_3$: black line), HS-Co^{3+} ($Sr_2Co^{3+}RuO_6$: green line), and $Co^{2+}O$ (blue line). c) Ru L_3-edge spectra of CCCRO (red line) and references $Sr_2CoRu^{5+}O_6$ (black line) and $SrRu^{4+}O_3$ (blue line). d) Cu *K*-edge spectra of CCCRO (red line) and references Cu^0 foil (green line), $Cu^{2+}O$ (black line), and $Cu^{+}{}_2O$ (blue line). e) Co *K*-edge spectra of CCCRO (red line) and references Co^0 foil (green line), $LaCo^{3+}O_3$ (black line), and $Co^{2+}O$ (blue line). f) Ru *K*-edge spectra of CCCRO (red line) and references $Sr_2GdRu^{5+}O_6$ (black line), $Ru^{4+}O_2$ (blue line), $Ru^{3+}Cl_3$ (purple line), and Ru^0 foil (green line). g–i) The EXAFS fitting curves for CCCRO. j–l) WT for the k^2-weighted EXAFS spectra of CCCRO.

the Co—O bond had a shorter length than the Ru—O bond because the Co ion had a smaller ionic radius than the Ru ion. Furthermore, the coordination conditions of Cu/Co/Ru were visually explored using a powerful wavelet transform (WT) analysis to directly reflect the structure information in the *R* and *K* spaces. The WT of CCCRO and reference samples supporting the EXAFS analysis are depicted in Figure 2j–l and Figure S10 (Supporting Information).

2.3. Electrocatalytic OER Performance

The OER performance of CCCRO was evaluated using electrochemical measurements in an O_2-saturated 1 M KOH solution with a standard three-electrode system. The electrode potentials were calibrated with respect to the reversible hydrogen electrode (RHE). A glassy carbon electrode (GCE) operated at 1600 rpm, and a 5 mV s^{-1} scan rate was employed for linear sweep

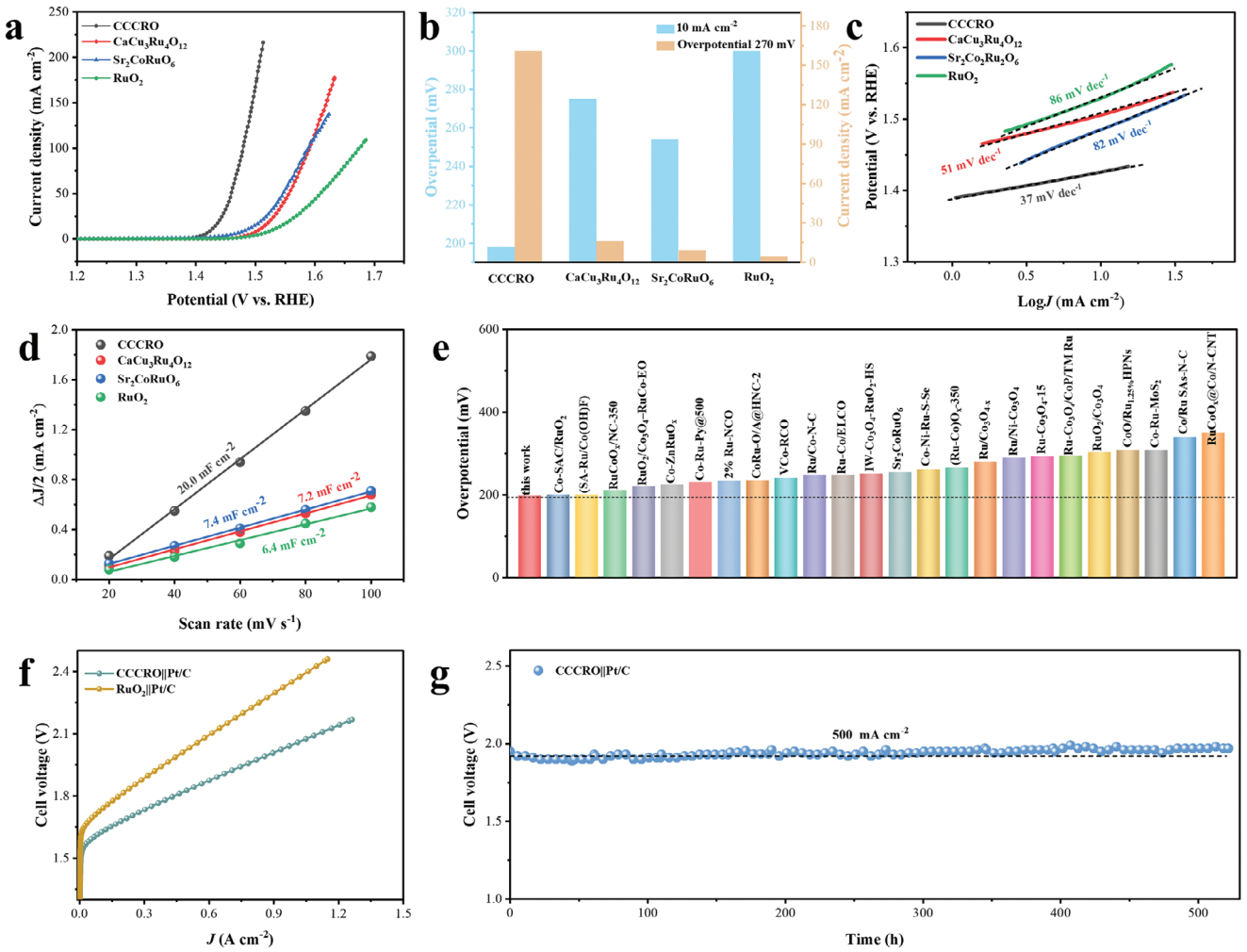

Figure 3. Electrocatalytic OER performance. a) LSV curves of CCCRO, $CaCu_3Ru_4O_{12}$, Sr_2CoRuO_6, and RuO_2. b) Comparison of the overpotentials (at current density of 10 mA cm^{-2}) and the current densities (at an overpotential of 270 mV) of the CCCRO, $CaCu_3Ru_4O_{12}$, Sr_2CoRuO_6, and RuO_2. c) Tafel plots. d) Differences in the charging current density plotted against the scan rate for CCCRO, $CaCu_3Ru_4O_{12}$, Sr_2CoRuO_6, and RuO_2. e) Comparison of the overpotential at 10 mA cm^{-2} for CCCRO and the previously reported Co-Ru based catalysts. f) LSV curves of the AEM electrolyzer using CCCRO and RuO_2, Pt/C catalysts as the anodic and cathodic electrodes, respectively. g) Stability tests of the AEM water electrolyzers at 500 mA cm^{-2}.

voltammetry (LSV). This study selected $CaCu_3Ru_4O_{12}$ and Sr_2CoRuO_6 as references since the OER activity could be checked in case of the lack of Co or Cu at the B or A sites, respectively. As shown in the LSV curve in **Figure 3a**, CCCRO had a low overpotential of only 198 mV to achieve a current density of 10 mA cm^{-2}, which surpassed the performance of $CaCu_3Ru_4O_{12}$ (275 mV), Sr_2CoRuO_6 (254 mV), $CaCu_3Co_4O_{12}$ (370 mV),[44] and commercial RuO_2 (300 mV). Additionally, at a 270 mV overpotential (+1.50 V vs RHE), CCCRO had a specific OER activity ≈10, 18, and 38 times higher than $CaCu_3Ru_4O_{12}$, Sr_2CoRuO_6, and commercial RuO_2, respectively (Figure 3b). A comparison of the mass activities (MA) of the CCCRO, $CaCu_3Ru_4O_{12}$, Sr_2CoRuO_6, and RuO_2 catalysts at 1.5 V (vs RHE) is shown Figure S11 (Supporting Information). CCCRO exhibited the highest MA of 788.9 A g^{-1}, ≈38 times higher than that of commercial RuO_2. Furthermore, Tafel analysis was used to gain a more comprehensive understanding of the OER kinetics, as shown in Figure 3c. CCCRO exhibited the lowest Tafel slope of 37 mV dec^{-1}. The Tafel slopes of $CaCu_3Ru_4O_{12}$, Sr_2CoRuO_6, $CaCu_3Co_4O_{12}$,[44] and RuO_2 were 51, 82, 75, and 86 mV dec^{-1}, respectively. Furthermore, electrochemical impedance spectroscopy (EIS) confirmed the enhanced charge transfer capability of CCCRO sample (Figure S12, Supporting Information). The electrochemically active surface area (ECSA), determined using the non-Faradaic cyclic voltammetry (CV) data exhibited a positive correlation with the electrochemical double layer capacitance (C_{dl}) (Figure S13, Supporting Information). As illustrated in Figure 3d, CCCRO had the largest ECSA and more electrochemically active sites, which were conducive to catalyzing OER. To further assess the intrinsic catalytic activities of samples, LSVs curves were further normalized by ECSA (Figure S14, Supporting Information), and CCCRO exhibited the highest intrinsic activity. Meanwhile, the intrinsic activity of the electrocatalysts was investigated using the turnover frequency (TOF). In comparison to its counterparts, CCCRO exhibited the highest TOF value for the OER (Figure S15, Supporting Information), thereby further confirming the highest

OER activity for CCCRO. A 100-h chronoamperometry confirmed that CCCRO had long-term stability without any significant loss of activity (Figure S16, Supporting Information). The electrochemical analysis mentioned earlier demonstrated that CCCRO had exceptional OER performance in alkaline conditions, surpassing numerous previously reported Co-Ru based electrocatalysts (Figure 3e; Table S4, Supporting Information).

Moreover, an anion exchange membrane (AEM) electrolyzer was constructed to investigate the potential applications of CCCRO under industrial conditions. The AEM electrolyzer had a sandwich structure with a 4 cm^2 surface area, and it comprised a collector, commercial 20% Pt/C as a cathode catalyst, CCCRO as an anode catalyst, and an anionic membrane, as shown in Figure S17 (Supporting Information). Additionally, an AEM electrolyzer with commercial RuO_2 as the anode catalyst was constructed. As depicted in Figure 3f, the CCCRO catalyst had cell voltages of 1.83 and 2.05 V at room temperature for current densities of 0.5 and 1.0 A cm^{-2}, respectively. In contrast, the RuO_2 catalyst had cell voltages of 2.02 and 2.37 V at current densities of 0.5 and 1.0 A cm^{-2}, respectively (Figure S18, Supporting Information). Furthermore, the long-term stability of the AEM electrolyzer at a 500 mA cm^{-2} current density was investigated. As illustrated in Figure 3e, CCCRO had considerable stability for >500 h with negligible potential fluctuations, suggesting promising prospects for industrial utilization.

2.4. In Situ Spectroscopic Studies on OER Mechanism

Synchrotron-based in situ XAS and XRD were used to gain a deep understanding of underlying OER mechanisms of CCCRO. The in situ Co-*K* XANES spectra as a function of the applied potential from the open circuit potential (OCP) to 1.75 V (vs RHE) are shown in **Figure 4**a,b. The absorption edge shifted to higher energy with the progressive rise in the potential, indicating an increased valence state of Co ions. The specific variation in the valence state of Co ions in response to applied potential was assessed in comparison with $LaCoO_3$ and $BaCoO_3$, the standard Co (III) and Co (IV) references, respectively (Figure 4c). The valence state of the Co ions reached its maximum value of approximately $Co^{+3.48}$ at an applied potential of 1.75 V. As reported in previous theoretical calculations, the Co (IV) oxidation state was primarily responsible for the high OER activity.[19,31] Furthermore, the possible change of the local coordination environment of the Co ion was investigated using the in situ EXAFS spectroscopy. The FT-EXAFS and the evolution of the Co—O bond length obtained through EXAFS fitting are illustrated in Figure 4d1,d2. The EXAFS fit curve and detailed data are presented in Figure S19 and Table S5 (Supporting Information). Evidently, the Co—O bond length decreased as the applied potential increased. Furthermore, the WT analysis of EXAFS showed no changes in the Co-O-Ca/Cu network under different potentials (Figure S20, Supporting Information).

The in situ *K*-edge XANES of Ru and Co for the CCCRO catalyst as a function of the applied potential exhibited similar trends. As depicted in Figure 4e,f, the absorption edge of the Ru *K*-edge XANES shifted towards higher energy with the increase in applied potential, indicating an increased valence state of the Ru ions. The in situ XANES spectra suggested that the hexavalent Ru (VI) ions were OER active species. In this study, Ru (VI) indicated a strong covalence of a very high oxidation state of Ru ion. As quantified by the $Ru^{4+}O_2$ and $Sr_2GdRu^{5+}O_6$ standard references, the change in the valence state of Ru ions under different potentials is illustrated in Figure 4g. As the applied potential increased, the valence state increased until it reached the highest valence state of $Ru^{+5.45}$. The FT-EXAFS of CCCRO as a function of the applied potential is shown in Figure 4h1. The first peak (≈1.45 Å) representing the Ru-O bond length shifted slightly leftward, indicating a contracted Ru—O bond length. The changes in the Ru—O bond length were quantified using the EXAFS data fitting, and the results are presented in Figure 4h2. The Ru—O bond length gradually decreased from 1.97 Å in the air to 1.93 Å at 1.45 V as the applied potential increased. However, the Ru—O bond length only slightly reduced over the 1.45–1.75 V applied potential range. The EXAFS fitting curves and detailed data are shown in Figure S21 and Table S6 (Supporting Information). Additionally, the WT results of the in situ Ru *K*-edge EXAFS demonstrated the absence of any structural change during OER (Figure S22, Supporting Information).

Furthermore, it was explored whether Cu ions would undergo a valence state transition as a function of the applied potential like Co and Ru ions. As shown in the in situ Cu-*K* XANES in Figure 4i, the absorption edge did not shift with the increase in the applied potential, indicating that the Cu^{2+} valence state remained unchanged and OER inactive for Cu ions in CCCRO. Additionally, as shown in the FT-EXAFS and detailed data fitting in Figures S23–S25 and Table S7 (Supporting Information), there were no changes in the local environment of the Cu ion. WT further confirmed no structural changes in the Cu ions under different potentials (Figure S26, Supporting Information).

Moreover, in situ XRD was measured using synchrotron radiations to confirm the structural stability of CCCRO under OER. As shown in Figure 4j, there were no additional diffraction peaks with the increase in the applied potential, and the intensity of the diffraction peaks of CCCRO did not change. Consequently, this indicated that the CCCRO catalyst maintained its structural stability under OER condition. Raman spectroscopy is a robust technique for surface characterization, and it enables the detection of several parameters, like crystal phase, chemical state, and structural distortion.[45–47] The in situ Raman spectroscopy did not indicate any of structural changes (Figure S27, Supporting Information). Thus, all in situ spectroscopic results concluded a high structural stability of CCCRO under OER, which was responsible for the OER operational stability observed for over 500 h.

From in situ XAS we know that the valence states of Co and Ru increase from Co^{3+}\$Ru^{5+}$ to $Co^{3.5+}$\$Ru^{5.5+}$, which can be understood by leaching of Ca and Cu ions found from EDX (Table S8, Supporting Information) and inductively coupled plasma-mass spectrometry (ICP-MS) (Table S9, Supporting Information). However, the SR-based XRD of CCCRO before and after OER in Figure S28 (Supporting Information) exhibited the same patterns with only slightly shift to the large angle. The Raman spectroscopy of CCCRO before and after OER confirmed negligible structural changes of CCCRO during OER, as shown in Figure S29 (Supporting Information). The HRTEM images

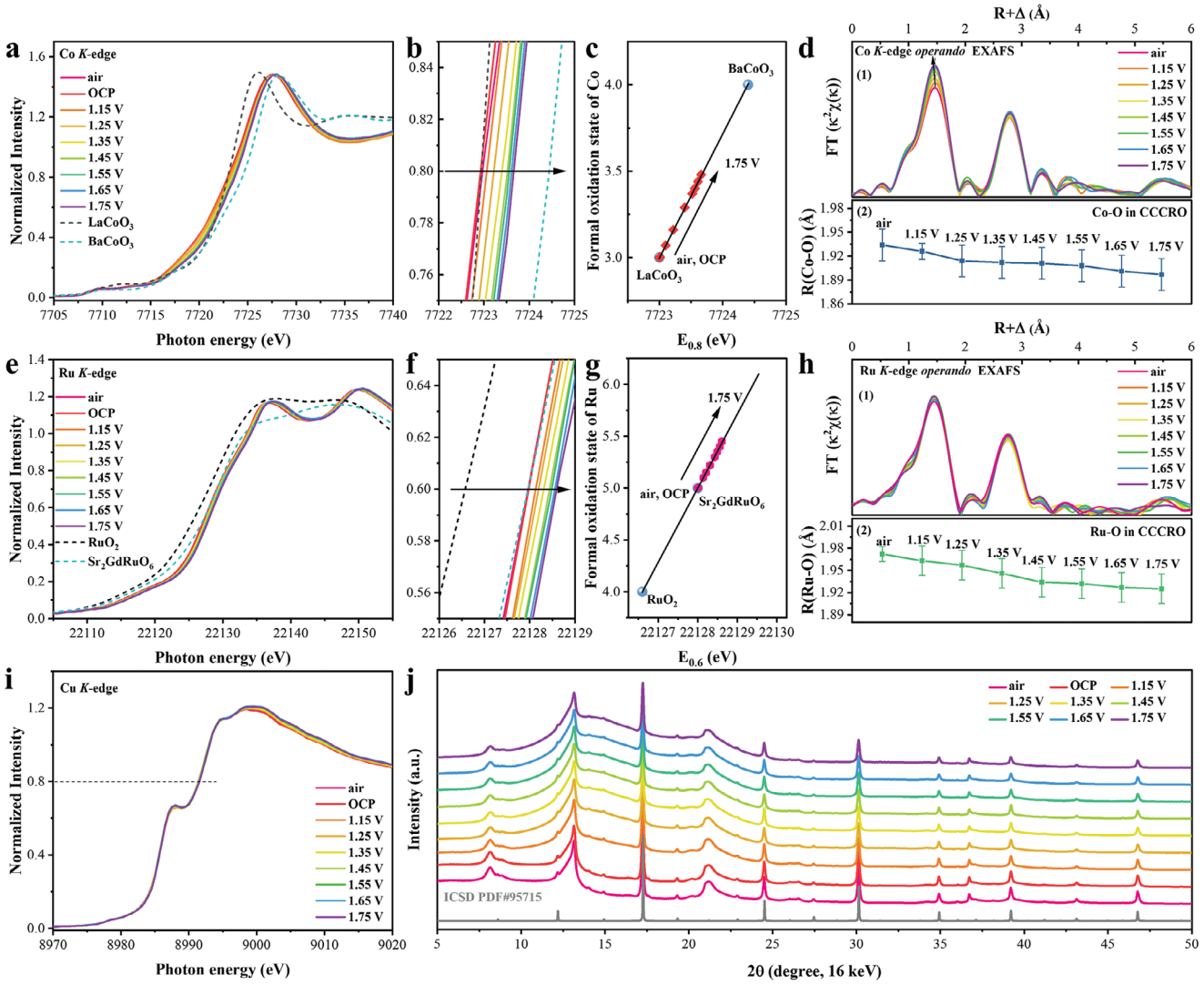

Figure 4. In situ spectra of CCCRO under different potentials. a,e,i) The *K*-edge XANES spectra of Co, Ru, and Cu for CCCRO at the applied potentials. b,f) The partially enlarged view of Co and Ru *K*-edge XANES. c,g) Oxidation states derived from (a,e), respectively. d1,h1) FT-EXAFS at the Co and Ru *K*-edges. d2,h2) Co-O and Ru-O bond lengths in the CCCRO electrocatalyst under the applied potentials, as extracted from the EXAFS fitting. The applied potential is referenced as RHE. j) In situ SR-based XRD patterns of CCCRO under the applied potentials.

taken after OER showed that crystal plane spacing (d = 0.264 nm) for the (220) crystal planes was consistent with that observed before OER (Figure S30, Supporting Information). Additionally, EDX images showed a uniform elemental distribution with no obvious element segregation after OER (Figure S31, Supporting Information). Additionally, HAADF-STEM confirmed that the atomic arrangement remained unchanged after OER (Figure S32, Support Information). Thus, all above results indicated that the crystal lattice of the remaining ions is unchanged. The *K*-edge spectra of Cu, Co, and Ru for CCCRO before and after OER demonstrated that there was no change in the valence state of Cu, Co, and Ru ions and in the crystal structural of the bulk of CCCRO (Figure S33, Supporting Information). Additionally, sXAS at the 3d elements $L_{2,3}$-edge taken with total electron yield (TEY) mode has a detection depth of ≈5 nm and therefore is sensitive to electronic structure of the surface. As shown in Figure S34 (Supporting Information), the Cu and Co $L_{2,3}$-edge spectra of CCCRO after the OER (green line) has the same energy as that of before the OER (red line) revealing no change in the valence states of Cu and Co ions. However, due to partial dissolution of Ca and Cu ions, there is a slight contraction of lattice leading to a spin state transition from HS-Co^{3+} to LS-Co^{3+} (Figure S34b, Supporting Information), as known from comparison of HS-Co^{3+} (Sr_2CoRuO_6)[40] and LS-Co^{3+} ($EuCoO_3$)[33] at the bottom of Figure S34b (Supporting Information). Moreover, the results of Ru L_3-edge shown that Ru returned to the +5 valence state after the OER (Figure S34c, Supporting Information). Therefore, it highlighted the importance of in situ techniques in identifying the real active sites.

2.5. DFT Calculations and the Electrocatalysis Mechanism

Considering that in situ XAS suggested that Co and Ru ions were OER active sites and Cu ion was relatively OER inactive in CCCRO catalysts, first-principles DFT was employed to gain further insights into the fundamental OER mechanism of CCCRO. The surface reaction pathway was simulated using BO_2-terminated (001) planes. Considering that the in situ XAS obtained the $Cu^{2+}/Co^{+3.5}/Ru^{+5.5}$ valence states and EDX derived the ratio of Ca and Cu after OER, the proposed model was $Ca_{0.5}Cu_{2.5}Co^{+3.5}{}_2Ru^{+5.5}{}_2O_{12}$ (Table S8, Supporting Information). The $Ca_{0.5}Ru^{+5.5}{}_2O_6$, $Ca_{0.5}Cu_{0.5}Ru^{+5.5}{}_4O_{12}$, and $Ca_{1.5}Co^{+3.5}Ru^{+5.5}O_6$ models were also considered for comparison (Figure S35, Supporting Information). The reaction mechanisms considered four proton-electron transfer steps and were both AEM and LOM, as shown in **Figure 5**a,b. The values of Gibbs free energy (ΔG) values for these structures obtained at $U_{RHE} = 0$ V potential using AEM and LOM pathways are shown in Figure 5c,d and Figure S36 (Supporting Information). Since the *OOH formation in $Ca_{0.5}Ru_2O_6$ under AEM route exhibited a higher free energy barrier, the theoretical thermodynamic overpotential (η) was 1.02 V (LOM gives 1.6 V), which served as the rate-determining step for OER. For the $Ca_{0.5}Cu_{0.5}Ru_4O_{12}$, the AEM route also has the lower overpotential than LOM path, and the η decreased to 0.78 V. Although Cu^{2+} was found to exhibit OER inactivity, the synergistic effects of Cu^{2+}-$Ru^{5.5+}$ could enhance the OER activity. This could be attributed to the optimized Ru 4d electronic structure due to the Cu 3d electrons through the Cu(A')-O-Ru(B) network, reducing the overpotential compared to Ca ($3d^0$) with 3d electrons.[20]

Under the AEM path, $Ca_{1.5}CoRuO_6$ had a slightly higher theoretical overpotential for OER (0.15 V at Co site and 0.10 V at Ru site). However, under the LOM path, $Ca_{1.5}CoRuO_6$ had theoretical overpotential values of 0.75 V (Co site) and 0.57 V (Ru site), which was lower than those of $Ca_{0.5}Ru_2O_6$ and $Ca_{0.5}Cu_{0.5}Ru_4O_{12}$ in AEM and LOM paths (Table S10, Supporting Information). We can conclude that LOM scenario represents the real OER mechanism for Co (IV)-O-Ru (VI) network in the similar way as Co (IV) and Ni (IV) oxides.[32,33] When the ions of all three TMs, Cu, Co and Ru in CCCRO were considered in the LOM pathway, the η values reduced to 0.32 V (Co site) and 0.38 V (Ru site), much lower than $\eta = 0.75$ V (Co site) and $\eta = 0.57$ V (Ru site) for the LOM pathway of the bimetallic $Ca_{1.5}CoRuO_6$ catalyst. These results further demonstrated that synergistic effects of the three TM ions efficiently boosted the OER activity in CCCRO, though Cu ions were relatively OER inactive. These values were smaller than $\eta = 0.77$ V (Co site) and $\eta = 0.68$ V (Ru site) for AEM pathway in CCCRO.

To gain further understanding of the origin of trimetal cooperatively enhanced OER activity by means of the participation of Cu 3d(A' site)-O-Co 3d/Ru 4d(B site) in bonding, we also investigated the low energy electronic structure close to Fermi energy (E_F) of $Ca_{1.5}CoRuO_6$, and Cu ions embedded in $Ca_{0.5}Cu_{2.5}Co_2Ru_2O_{12}$. In $Ca_{1.5}CoRuO_6$, there is an overlap between Co 3d/Ru 4d states with O 2p at the Fermi energy (E_F) in Figure 5e. As Cu ions is embedded in CCCRO, the density state of total d character close to at E_F (black line in Figure 5f) increases very clearly. This result demonstrates that inactive Cu species can optimize the electronic structure at the E_F, in turn improve the OER performance in CCCRO. Thus, the microelectronic origin of the synergistic effects among three sites (Cu, Co, and Ru) can be well understood.

To confirm the involvement of lattice oxygen during OER, we assessed the pH dependence of the CCCRO. LSV curves were obtained at different pH values (13.7, 13.5, and 13.0), as shown in Figure S37 (Supporting Information). CCCRO exhibited pronounced dependence to pH values. The implication here was the involvement of non-cooperative proton-electron transfer and LOM pathway in the OER, rather than the conventional AEM pathway. Moreover, we conducted ^{18}O-isotope labelling experiments using in situ differential electrochemical mass spectrometry (DEMS). First, the experiment was carried out on more than four consecutive CV cycles of unlabeled CCCRO in an ^{18}O-enriched 0.1 M KOH electrolyte (Figure S38, Supporting Information). After partial replacement of lattice ^{16}O by ^{18}O from the electrolyte, the ^{18}O-labeled CCCRO was cycled through another four cycles in $H_2{}^{16}O$-based KOH electrolyte to investigate whether lattice oxygen participated in the OER (Figure 5g). The results of the CV cycles demonstrated that the ^{18}O-labeled CCCRO exhibited abundances exceeding 1.5 times the natural isotope abundance in the water (Figure 5h), indicating participation of lattice oxygen via LOM pathway.

3. Conclusion

A new electrocatalyst of composite perovskite oxide, CCCRO was successfully synthesized. The CCCRO catalyst exhibits best OER performance and prolonged operational stability among Co-Ru catalysts. The CCCRO catalyst have Cu^{2+}, Co^{3+}, and Ru^{5+} states, as determined using the ex situ XAS spectra at the Cu-$L_{2,3}$ (Cu-*K*), and Co-$L_{2,3}$ (Co-*K*), and Ru-*L* (Ru-*K*) edges, respectively. The in situ XANES spectra, as a function of applied potential, indicated that nearly half of Co^{3+} and Ru^{5+} ions were transferred to the Co (IV) and Ru (VI) valence states, respectively. However, the Cu^{2+} valence state remained unchanged. Furthermore, various in situ techniques, such as EXAFS, XRD, and Raman spectroscopy, showed that CCCRO maintained its structural stability during OER. The conclusions drawn from DFT calculations are as follows: (1) Rather than the conventional AEM, the LOM path similar to that for Co (IV)/Ni (IV) oxides, was a real OER mechanism in CCCRO. (2) Cu^{2+} was relatively OER inactive, but it optimized the electronic structure through the A'-O-B/B' path to enhance the OER activity as further confirmed by density state close to E_F. This study presents a highly efficient OER catalyst and a deep understanding of the underlying mechanism of multisite synergistic effects of OER.

4. Experimental Section

Synthesis of the CCCRO Catalysts: The high temperature and high pressure (HPHT) method was used to synthesize perovskite CCCRO materials. The starting materials were high-purity CaO, CuO, Co_3O_4, RuO_2, and $KClO_4$ powders, which were thoroughly mixed in an agate mortar at a molar ratio of 3: 9: 2: 6: 3. Subsequently, the mixture was sealed into a platinum capsule and subjected to HPHT treatment at 8 GPa and 1550 K for 30 min on a cubic-anvil-type apparatus. The sample was rapidly cooled to room temperature after the heat treatment, followed by the gradual release of the pressure. Finally, the resulting polycrystalline pellet was rinsed with deionized water to eliminate the residual KCl.

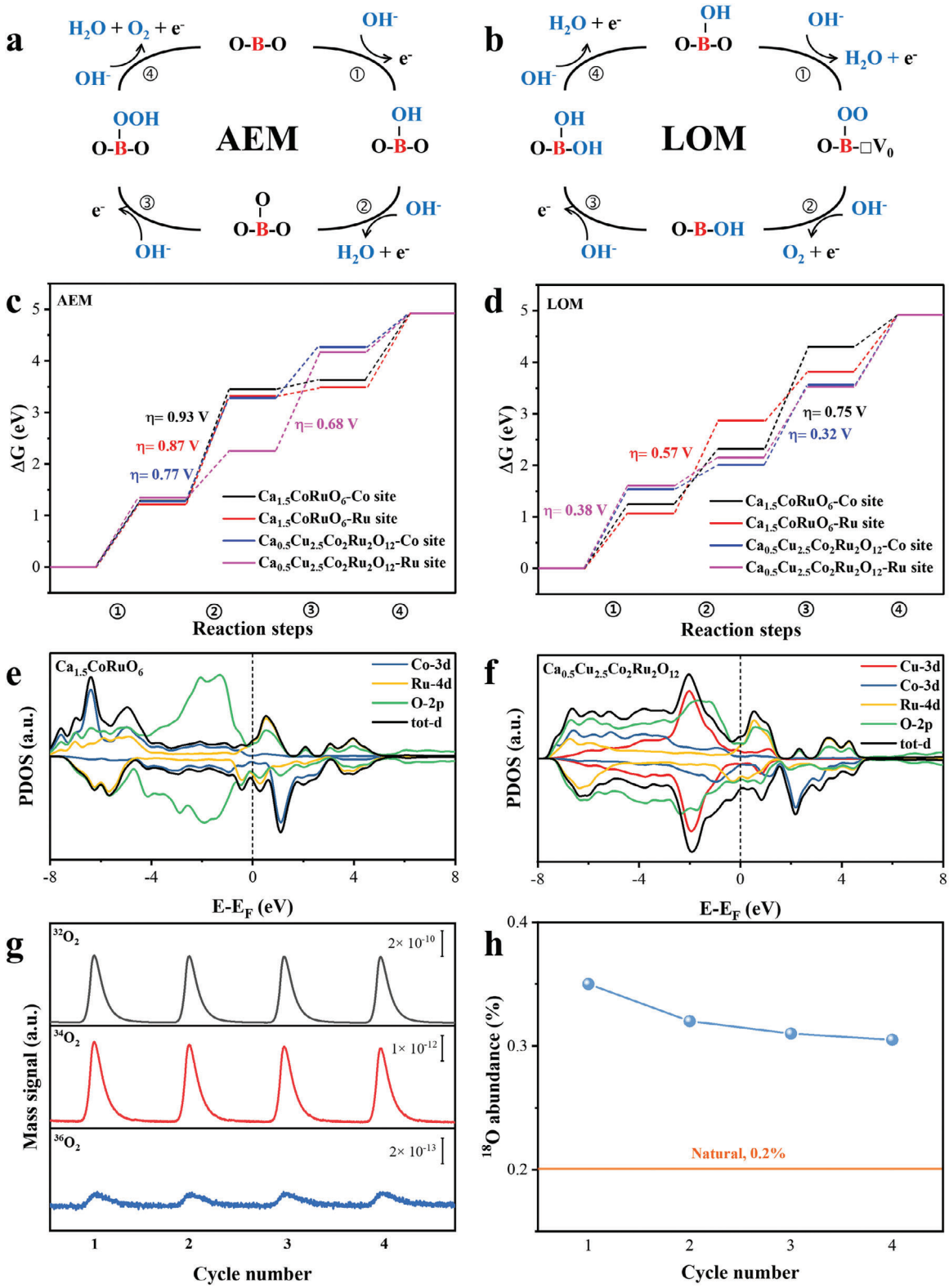

Figure 5. The OER mechanism of CCCRO. a) AEM, the letter B represents the element at the B-position in perovskite, which consists of Co and Ru in CCCRO. b) LOM. c,d) AEM and LOM on $Ca_{1.5}CoRuO_6$ and $Ca_{0.5}Cu_{2.5}Co_2Ru_2O_{12}$, respectively. e,f) Projected density of states of $Ca_{1.5}CoRuO_6$ and $Ca_{0.5}Cu_{2.5}Co_2Ru_2O_{12}$. The Fermi levels are set to 0 eV. g) DEMS results by ^{18}O-isotopic labeled CCCRO with CV cycles in $H_2{}^{16}O$-based 0.1 M KOH electrolyte. h) The evolution of measured ^{18}O abundance of evolved oxygen (from total DEMS charge) for ^{18}O-labled CCCRO with CV cycles.

Synthesis of the $CaCu_3Ru_4O_{12}$ and Sr_2CoRuO_6 Catalysts: A conventional solid-state reaction was used to prepare the $CaCu_3Ru_4O_{12}$ and Sr_2CoRuO_6 powders. For $CaCu_3Ru_4O_{12}$, a mixture of $CaCO_3$, CuO, and RuO_2 in a 1:3:4 molar ratio was sintered at 1273 K for 24 h in the air. The purity of the phase was confirmed using XRD, and the desired results were achieved using multiple sintering rounds. For Sr_2CoRuO_6, a mixture of $SrCO_3$, Co_3O_4, and RuO_2 in a 6:1:3 molar ratio was used as the starting material, which was calcined at 1473K for 24 h in the air. The purity of the phase was confirmed using XRD, and the desired results were achieved using multiple rounds of sintering.[48]

Commercial RuO_2, Pt/C Catalysts: RuO_2 and 20% Pt/C was purchased from Aladdin.

Structural Characterization: The structure of the catalyst was determined using XRD (Bruker D8 Advance X-ray diffractometer). The structure was refined using Rietveld refinement in the general structure analysis system (GSAS).[49] An excitation wavelength of 473 nm was used for the in situ Raman spectroscopy (Horiba LabRAM HR Evolution). The in situ Raman measurements were performed in 1 M KOH, and the other conditions were the same as those used for electrochemical activation. The morphology of the materials was visualized using TEM (FEI Tecnai-G2 F20) with a 200 kV acceleration. HAADF-STEM images were recorded using an aberration-corrected microscope (FEI Themis Z STEM), which was operated at a 60 kV accelerating voltage. The angle range of the HAADF detector was 50–200 mrad. In situ Cu/Co and Ru *K*-edge XAS spectra were acquired at the Shanghai Synchrotron Radiation Facility (SSRF) in the fluorescence mode with a Si(111) double-crystal monochromator at the BL20U beamline and in fluorescence mode with a Si(311) double-crystal monochromator at the BL 14W1 beamline, respectively.[50] All *K*-edge XAS data were analyzed using the program Demeter.[51] The energy calibration was according to the absorption edge of the Cu/Co/Ru foil. The sXAS at the Cu $L_{2,3}$-edge and the Co $L_{2,3}$-edge were collected at TLS 11 A of the National Synchrotron Radiation Research Centre (NSRRC). Due to the low photon energy of soft XAS, the sample and the single crystal CuO (CoO) were measured at the same time for energy correction to ensure data accuracy. The Ru L_3-edge was collected at the TLS 16 A of the NSRRC. The SR-based XRD patterns were collected at the TLS 01C2 beamline of the NSRRC. The incident beam energy for the XRD experiments was 16 keV, and a CeO_2 reference sample was used to calibrate the diffraction intensity and the peak shape.

Electrochemical Measurements: OER was performed in O_2-saturated 1 M KOH using a three-electrode system on an electrochemical workstation (Metrohm Autolab equipped with a PGSTAT 302 N system). First, 5 mg of the catalyst powder and 5 mg of the carbon black were dispersed in a solution of deionized water (700 µL) and isopropanol (250 µL). Then, 40 µL of Nafion was then added to the mixture, which was placed in an ultrasonic water bath for 1 h. Then, 8 µL of the resulting catalyst ink was added dropwise onto the polished GCE, and the working electrode was allowed to dry naturally before testing. A Hg/ HgO electrode served as the reference electrode, and the GCE with a 5 mm diameter (0.196 cm^2) was used as the working electrode. The potential equation with RHE was $E(\mathrm{RHE}) = E(\mathrm{Hg/HgO}) + 0.059*\mathrm{pH} + 0.0977$ V. The resistance compensation was based on manual iR-correction. The 1 M KOH aqueous solution had a pH value of 13.72 at room temperature. The frequency range for the impedance spectroscopy analysis was 10^5 Hz-10^{-2} Hz. The geometric area of the AEM electrolyzer was 4 $cm^{[2]}$ (2 cm × 2 cm). The cathode and anode inks were evenly sprayed onto both sides of the surface of Fumasep FAA-3-PK-75 ionic membrane, with a loading capacity of 1.0 mg cm^{-2}.

Computation Details: Spin-polarization first principles DFT calculations with the Vienna ab-initio simulation program (VASP) were employed to simulate the electronic properties and Gibbs free energy for OER process.[52,53] The calculation was performed within the framework of generalized gradient approximation, employing the Perdew–Burke–Ernzerh formula.[54] The valence electrons considered were H $1s^1$, O $2s^2 2p^4$, Co $4s^2 3d^7$, Cu $4s^1 3d^{10}$, and Ru $5s^1 4d^7$. The Hubbard U model was incorporated to describe the strong correlation effects in local Co 3d states to address the self-interaction error of the exchange-correlation function. This study sets U_{eff} = (U−J) to be 3.52 eV.[19] A vacuum spacing perpendicular to the structural plane of 15 Å wa employed to eliminate spurious interactions, and Brillouin zone integration was performed with a 3 × 3 × 1 Monkhorst–Pack k-point mesh.[55] The projected augmentation wave potential was chosen to describe the ionic nucleus while considering the valence electrons using a plane wave basis set. The kinetic energy cutoff was set at 520 eV. The utilization of the Methfessel-Paxton smearing method with a 0.02 eV width allowed for a partial occupation of the Kohn-Sham orbitals. The electronic energy was considered self-consistent when the energy change was less than 10^{-5} eV. The ΔG values for these intermediates included the zero-point energy (ZPE) and the entropy correction terms according to the formula: $\Delta G = \Delta E + \Delta ZPE - T\Delta S$, where ΔE represents the energy difference calculated relative to H_2O (l) and H_2 (g) (at $U_{RHE} = 0$).

Supporting Information

Supporting Information is available from the Wiley Online Library or from the author.

Acknowledgements

Y.F. and X.Y. contributed equally to this work. This work was supported by the Strategic Priority Research Program of the Chinese Academy of Sciences (No. XDA0400000), the National Key R&D Program of China (2021YFA1502400 and 2022YFB4002502), the National Science Foundation of China (Grant No. 22179141 and 12304268), the Shanghai Municipal Science and Technology Program (Grant No. 21DZ1207700), the Photon Science Center for Carbon Neutrality, and the Talent Plan of Shanghai Branch, the Chinese Academy of Sciences (CASSHB-QNPD-2023-006). The authors acknowledge support from the Max Planck-POSTECH-Hsinchu Center for Complex Phase Materials. The National Key R&D Program of China (2021YFA1400300), the National Science Foundation of China (Grant No. 12425403, 11934017, and 11921004), the China Postdoctoral Science Foundation (Grant No. 2023M743741). [Correction added on December 7, 2024, after first online publication: Acknowledgement Section has been updated.]

Open access funding enabled and organized by Projekt DEAL.

Conflict of Interest

The authors declare no conflict of interest.

Data Availability Statement

The data that support the findings of this study are available from the corresponding author upon reasonable request.

Keywords

in situ XAS, multi-sites synergistic effects, oxygen evolution reaction

Received: October 4, 2024
Revised: November 14, 2024
Published online:

[1] Z. W. Seh, J. Kibsgaard, C. F. Dickens, I. Chorkendorff, J. K. Nørskov, T. F. Jaramillo, *Science* **2017**, *355*, eaad4998.
[2] S. Chu, A. Majumdar, *Nature* **2012**, *488*, 294.
[3] I. Katsounaros, S. Cherevko, A. R. Zeradjanin, K. J. Mayrhofer, *Angew. Chem., Int. Ed.* **2014**, *53*, 102.

[4] F. Song, L. Bai, A. Moysiadou, S. Lee, C. Hu, L. Liardet, X. Hu, *J. Am. Chem. Soc.* **2018**, *140*, 7748.
[5] X. Yang, C. P. Nielsen, S. Song, M. B. McElroy, *Nat. Energy* **2022**, *7*, 955.
[6] A. Odenweller, F. Ueckerdt, G. F. Nemet, M. Jensterle, G. Luderer, *Nat. Energy* **2022**, *7*, 854.
[7] Y. Hu, L. Li, J. Zhao, Y.-C. Huang, C.-y. Kuo, J. Zhou, Y. Fan, H.-J. Lin, C.-L. Dong, C.-W. Pao, J.-F. Lee, C.-T. Chen, C. Jin, Z. Hu, J.-Q. Wang, L. Zhang, *Appl. Catal. B-Environ.* **2023**, *333*, 122785.
[8] Y. Fan, C. Zhang, L. Zhang, J. Zhou, Y. Li, Y.-C. Huang, J. Ma, T.-S. Chan, C.-T. Chen, C. Jing, E. Mijit, Z. Hu, J.-Q. Wang, L. Zhang, *Chem. Catal.* **2024**, *4*, 5.
[9] J. Ding, Q. Shao, Y. Feng, X. Huang, *Nano Energy* **2018**, *47*, 1.
[10] T. Ma, H. Cao, S. Li, S. Cao, Z. Zhao, Z. Wu, R. Yan, C. Yang, Y. Wang, P. A. van Aken, *Adv. Mater.* **2022**, *34*, 2206368.
[11] J. Zhao, H. Guo, Q. Zhang, Y. Li, L. Gu, R. Song, *Appl. Catal. B-Environ.* **2023**, *325*, 122354.
[12] Y. Hu, Y. Fan, L. Li, J. Zhou, Z. Hu, J. Q. Wang, J. Dong, S. Zhao, L. Zhang, *Small* **2024**, *2400042*, 20.
[13] Y. Zhu, H. A. Tahini, Z. Hu, Y. Yin, Q. Lin, H. Sun, Y. Zhong, Y. Chen, F. Zhang, H.-J. Lin, C.-T. Chen, W. Zhou, X. Zhang, S. C. Smith, Z. Shao, H. Wang, *EcoMat* **2020**, *2*, e12021.
[14] J. Hwang, R. R. Rao, L. Giordano, Y. Katayama, Y. Yu, Y. Shao-Horn, *Science* **2017**, *358*, 751.
[15] L. C. Seitz, C. F. Dickens, K. Nishio, Y. Hikita, J. Montoya, A. Doyle, C. Kirk, A. Vojvodic, H. Y. Hwang, J. K. Norskov, T. F. Jaramillo, *Science* **2016**, *353*, 1011.
[16] S. She, Y. Zhu, Y. Chen, Q. Lu, W. Zhou, Z. Shao, *Adv. Energy Mater.* **2019**, *9*, 1900429.
[17] L. Tang, Z. Chen, F. Zuo, B. Hua, H. Zhou, M. Li, J. Li, Y. Sun, *Chem. Eng. J.* **2020**, *401*, 126082.
[18] M. Retuerto, F. Calle-Vallejo, L. Pascual, G. Lumbeeck, M. T. Fernandez-Diaz, M. Croft, J. Gopalakrishnan, M. A. Peña, J. Hadermann, M. Greenblatt, S. Rojas, *ACS Appl. Mater. Interfaces* **2019**, *11*, 21454.
[19] L. Li, H. Sun, Z. Hu, J. Zhou, Y. C. Huang, H. Huang, S. Song, C. W. Pao, Y. C. Chang, A. C. Komarek, H.-J. Lin, C.-T. Chen, C.-L. Dong, J.-Q. Wang, L. Zhang, *Adv. Funct. Mater.* **2021**, *31*, 2104746.
[20] X. Ye, S. Song, L. Li, Y.-C. Chang, S. Qin, Z. Liu, Y.-C. Huang, J. Zhou, L.-j. Zhang, C.-L. Dong, C.-W. Pao, H.-J. Lin, C.-T. Chen, Z. Hu, J.-Q. Wang, Y. Long, *Chem. Mater.* **2021**, *33*, 9295.
[21] Z. Fan, Y. Ji, Q. Shao, S. Geng, W. Zhu, Y. Liu, F. Liao, Z. Hu, Y.-C. Chang, C.-W. Pao, Y. Li, Z. Kang, M. Shao, *Joule* **2021**, *5*, 3221.
[22] J. Dai, Y. Zhu, H. A. Tahini, Q. Lin, Y. Chen, D. Guan, C. Zhou, Z. Hu, H.-J. Lin, T.-S. Chan, C.-T. Chen, S. C. Smith, H. Wang, W. Zhou, Z. Shao, *Nat. Commun.* **2020**, *11*, 5657.
[23] W. Zhang, M. Xue, X. Zhang, C. Si, C. Tai, Q. Lu, M. Wei, X. Han, J. Ma, S. Chen, E. Guo, *Appl. Surf. Sci.* **2024**, *664*, 160278.
[24] P. Zhu, W.-X. Shi, Y. Wang, Z.-M. Zhang, L. Li, C. An, *Nano Res.* **2023**, *16*, 6593.
[25] X. Zheng, J. Yang, Z. Xu, Q. Wang, J. Wu, E. Zhang, S. Dou, W. Sun, D. Wang, Y. Li, *Angew. Chem., Int. Ed.* **2022**, *61*, e202205946.
[26] J. Wang, Y. Gao, H. Kong, J. Kim, S. Choi, F. Ciucci, Y. Hao, S. Yang, Z. Shao, J. Lim, *Chem. Soc. Rev.* **2020**, *49*, 9154.
[27] A. Grimaud, O. Diaz-Morales, B. Han, W. T. Hong, Y.-L. Lee, L. Giordano, K. A. Stoerzinger, M. T. Koper, Y. Shao-Horn, *Nat. Chem.* **2017**, *9*, 457.
[28] N. Zhang, Y. Chai, *Energy Environ. Sci.* **2021**, *14*, 4647.
[29] J. T. Mefford, X. Rong, A. M. Abakumov, W. G. Hardin, S. Dai, A. M. Kolpak, K. P. Johnston, K. J. Stevenson, *Nat. Commun.* **2016**, *7*, 11053.
[30] Q. Huang, G.-J. Xia, B. Huang, D. Xie, J. Wang, D. Wen, D. Lin, C. Xu, L. Gao, Z. Wu, J. Wu, F. Xie, W. Guo, R. Zou, *Energy Environ. Sci.* **2024**, *17*, 5260.
[31] J. Zhou, L. Zhang, Y.-C. Huang, C.-L. Dong, H.-J. Lin, C.-T. Chen, L. Tjeng, Z. Hu, *Nat. Commun.* **2020**, *11*, 1984.
[32] H. Huang, Y.-C. Chang, Y.-C. Huang, L. Li, A. C. Komarek, L. H. Tjeng, Y. Orikasa, C.-W. Pao, T.-S. Chan, J.-M. Chen, S.-C. Haw, J. Zhou, Y. Wang, H.-J. Lin, C.-T. Chen, C.-L. Dong, C.-Y. Kuo, J.-Q. Wang, Z. Hu, L. Zhang, *Nat. Commun.* **2023**, *14*, 2112.
[33] Y. Chin, Z. Hu, H.-J. Lin, S. Agrestini, J. Weinen, C. Martin, S. Hébert, A. Maignan, A. Tanaka, J. Cezar, N. Brookes, Y.-F. Liao, K.-D. Tsuei, C. Chen, D. Khomskii, L. Tjeng, *Phys. Rev. B* **2019**, *100*, 205139.
[34] C.-F. Chang, Z. Hu, H. Wu, T. Burnus, N. Hollmann, M. Benomar, T. Lorenz, A. Tanaka, H.-J. Lin, H. Hsieh, C. Chen, L. Tjeng, *Phys. Rev. Lett.* **2009**, *102*, 116401.
[35] Z. Hu, H. Wu, T. Koethe, S. Barilo, S. Shiryaev, G. Bychkov, C. Schüßler-Langeheine, T. Lorenz, A. Tanaka, H. Hsieh, H.-J. Lin, C. Chen, N. Brookes, S. Agrestini, Y.-Y. Chin, M. Rotter, L. Tjeng, *New J. Phys.* **2012**, *14*, 123025.
[36] Z. Hu, H. Wu, M. Haverkort, H. Hsieh, H.-J. Lin, T. Lorenz, J. Baier, A. Reichl, I. Bonn, C. Felser, A. Tanaka, C. Chen, L. Tjeng, *Phys. Rev. Lett.* **2004**, *92*, 207402.
[37] N. Hollmann, Z. Hu, M. Valldor, A. Maignan, A. Tanaka, H. Hsieh, H.-J. Lin, C. Chen, L. Tjeng, *Phys. Rev. B—Condens.* **2009**, *80*, 085111.
[38] T. Burnus, Z. Hu, H. Wu, J. Cezar, S. Niitaka, H. Takagi, C. F. Chang, N. B. Brookes, H.-J. Lin, L. Jang, A. Tanaka, K. Liang, C. Chen, L. Tjeng, *Phys. Rev. B—Condens.* **2008**, *77*, 205111.
[39] L. Tjeng, C. Chen, S. Cheong, *Phys. Rev. B* **1992**, *45*, 8205.
[40] J.-M. Chen, Y.-Y. Chin, M. Valldor, Z. Hu, J.-M. Lee, S.-C. Haw, N. Hiraoka, H. Ishii, C.-W. Pao, K.-D. Tsuei, J.-F. Lee, H.-J. Lin, L.-Y. Jang, A. Tanaka, C.-T. Chen, L. Tjeng, *J. Am. Chem. Soc.* **2014**, *136*, 1514.
[41] J. Zhou, Y. Hu, Y.-C. Chang, Z. Hu, Y.-C. Huang, Y. Fan, H.-J. Lin, C.-W. Pao, C.-L. Dong, J.-F. Lee, C.-T. Chen, J.-Q. Wang, L. Zhang, *ACS Catal.* **2022**, *12*, 3138.
[42] X. Lin, Y.-C. Huang, Z. Hu, L. Li, J. Zhou, Q. Zhao, H. Huang, J. Sun, C.-W. Pao, Y.-C. Chang, H.-J. Lin, C.-T. Chen, C.-L. Dong, J.-Q. Wang, L. Zhang, *J. Am. Chem. Soc.* **2021**, *144*, 416.
[43] L.-J. Zhang, J.-Q. Wang, J. Li, J. Zhou, W.-P. Cai, J. Cheng, W. Xu, G. Yin, X. Wu, Z. Jiang, S. Zhang, Z.-Y. Wu, *Chem. Commun.* **2012**, *48*, 91.
[44] T. Uyama, Y. Okazaki, S. Kawaguchi, I. Yamada, *ACS Appl. Energy Mater.* **2022**, *5*, 214.
[45] J.-C. Dong, X.-G. Zhang, V. Briega-Martos, X. Jin, J. Yang, S. Chen, Z.-L. Yang, D.-Y. Wu, J. M. Feliu, C. T. Williams, Z.-Q. Tian, J.-F. Li, *Nat. Energy* **2019**, *4*, 60.
[46] C. Jing, T. Yuan, L. Li, J. Li, Z. Qian, J. Zhou, Y. Wang, S. Xi, N. Zhang, H.-J. Lin, C.-T. Chen, Z. Hu, D.-W. Li, L. Zhang, J.-Q. Wang, *ACS Catal.* **2022**, *12*, 10276.
[47] Y. Hu, J. Zhou, L. Li, Z. Hu, T. Yuan, C. Jing, R. Liu, S. Xi, H. Jiang, J.-Q. Wang, L. Zhang, *J. Mater. Chem. A* **2022**, *10*, 602.
[48] S. Kim, P. Battle, *J. Solid State Chem.* **1995**, *114*, 174.
[49] A. C. Larson, R. B. Dreele, B. Toby, General Structure Analysis System-GSAS/EXPGUI **1994**, *748*.
[50] H. Yu, X. Wei, J. Li, S. Gu, S. Zhang, L. Wang, J. Ma, L. Li, Q. Gao, R. Si, F. Sun, Y. Wang, F. Song, H. Xu, X. Yu, Y. Zou, J.-Q. Wang, Z. Jiang, Y. Huang, *Nucl. Sci. Tech.* **2015**, *26*, 5.
[51] B. Ravel, M. Newville, *J. Synchrotron Radiat* **2005**, *12*, 537.
[52] G. Kresse, J. Furthmüller, *Phys. Rev. B* **1996**, *54*, 11169.
[53] G. Kresse, D. Joubert, *Phys. Rev. B* **1999**, *59*, 1758.
[54] J. P. Perdew, K. Burke, M. Ernzerhof, *Phys. Rev. Lett.* **1996**, *77*, 3865.
[55] H. J. Monkhorst, J. D. Pack, *Phys. Rev. B* **1976**, *13*, 5188.